

Transition to turbulence in shear flows



**POLITECNICO
DI TORINO**

Author: Pierluigi Pertoso

Supervisor: Prof.ssa Stefania Scarsoglio

Department of Mechanics and Aerospace Engineering

September 23, 2019

Ringraziamenti

Desidero ringraziare innanzitutto la mia tutor professoressa Stefania Scarsoglio, che mi ha seguito con professionalità, disponibilità e attenzione durante la stesura del lavoro.

Grazie alla mia famiglia, che mi ha fatto sentire a casa anche quando ero a 947 km di distanza. Ai miei genitori, per aver sempre creduto in me, per l'amore donatomi ogni singolo giorno, per avermi dato la libertà di scegliere il mio futuro, guidandomi ovunque andassi. Ad Ale e Bea, che mi hanno sopportato e sopportato come solo due sorelle sanno fare.

Grazie ad Anna, il cui amore è riuscito ad andare oltre la distanza che ci separava. Un punto di riferimento, sempre presente, sempre pronta a riabbracciarmi una volta tornato a casa.

Grazie a tutti i miei amici che mi hanno accompagnato in questo percorso. Agli amici storici di Andria, pilastri fondamentali nella mia vita e ai miei compagni di avventura, con cui ho condiviso questi meravigliosi anni qui a Torino. Grazie ai miei coinquilini, che si sono avvicinati durante i tre anni: grazie a Loris e ai ragazzi del secondo piano "Queo bon".

*I am an old man now, and when I die and go to heaven,
there are two matters on which I hope for enlightenment.
One is quantum electrodynamics and the other is the turbulent motion of fluids.
About the former, I am really rather optimistic.*

-Sir **Horace Lamb**, Fellow of the Royal Society

Abstract

Pipe flow is a prominent example among the shear flows that undergo transition to turbulence through the generation of some unstable structures.

Over the course of the last two centuries many studies have highlighted the importance of these exact coherent structures, called puffs and slugs, in the mechanism that bring to turbulence.

The aim of this thesis is to follow the “life” of these structures.

Their **birth**, caused experimentally by jet injection or naturally by an obstacle or by wall roughness. Fundamental is to understand how they are organized around exact coherent structures known as *travelling waves* and how their structure changes with Reynolds number.

Their **growth**, through splitting and spreading upstream and downstream. Fundamental is to find out what is the influence of the Reynolds number and how energy is distributed.

Their **death** (eventually), that brings the flow to relaminarize. Fundamental is to study lifetime in order to predict if and when turbulence will decay.

Finally, we summarize the main strategies useful to eliminate or at least control turbulence spreading.

Contents

1	Introduction	1
1.1	Introduction to turbulence	1
1.2	Reynolds number	1
1.3	Dynamics of pipe flow	2
2	Turbulent coherent structures (Birth)	6
2.1	Puffs, Slugs and Travelling Waves	6
2.2	Setup of experiments	7
2.3	Experimental and numerical results	9
3	Turbulent fronts propagation (Growth)	13
3.1	Puff splitting ($Re \leq 2300$)	14
3.2	Slug spreading ($Re > 2400$)	18
3.3	Energy budget at the fronts	20
4	Turbulent lifetime (Death)	22
4.1	Introduction to dynamical system theory	22
4.2	Distribution of lifetimes	24
5	How to eliminate turbulence	28
5.1	Friction losses	28
5.2	Turbulence control strategies	29
6	Conclusions	32
A	Appendix	34
	References	35

1 Introduction

1.1 Introduction to turbulence

Turbulence is one of the most common examples of complex and disordered dynamical behaviour in nature. It is commonly observed in everyday phenomena such as most of the terrestrial atmospheric circulation, river flows, smoke rising from a cigarette and even blood flowing in arteries.

Experimentally it has been observed that, by changing some parameters, flow undergoes a transition from laminar to turbulent. Generally, the motion of fluids is laminar at low speeds and becomes turbulent as the velocity increases.

In the laminar case, fluid flows regularly, smoothly and in parallel layers, with no disrupting between those layers. In this state, viscous forces are dominant.

On the other hand, when turbulence is triggered, fluid becomes disordered, chaotic and layers start mixing. Here, flow is dominated by inertial forces since velocity is higher.

In natural and industrial processes, turbulence can have unfavorable and even detrimental effects. Turbulence is the major cause of friction losses in transport processes and it is responsible for a drastic drag increase in flows over bounding surfaces. In general, the transfert of fluids is energetically far more efficient if the motion is smooth and laminar. Hence, much effort is invested into developing ways to control and reduce turbulence intensities, for instance by smoothing or cooling the walls of pipes or airfoils or by creating favorable pressure gradients.

Even more critical is the transition regime since the pressure and flow rate fluctuations in the laminar-turbulent intermittent flows are very large (markedly higher than in the case of a fully turbulent flow).

A more detailed discussion about friction losses is developed in the Chapter 5.

1.2 Reynolds number

The dimensionless quantity used as a guide is the **Reynolds number** (Re), defined as the ratio of inertial forces to viscous forces within a fluid which is subjected to relative internal movement due to different fluid velocities, which is known as a boundary layer in the case of a bounding surface such as the interior of a pipe.

This concept was introduced by *George Stokes* in 1851, but the Reynolds number was named after *Osborne Reynolds (1842–1912)*, who popularized its use in 1883 [3], after his pioneering study on the motion of fluids.

This fundamental parameter is used to estimate the likelihood of a flow to be

turbulent. Indeed, when the flow is characterized by a low Reynolds number, it is well-ordered and stable (hence, laminar), but when we increase it, the laminar flow gives way to highly disordered turbulent dynamics.

Furthermore, this dimensionless number can be used to predict a critical point, called the *transition point*, upstream of which the flow is fully laminar and downstream of which the flow is fully turbulent.

Actually, as it will be completely explained in the following chapter, the transition from laminar to turbulent flow takes place over a finite region.

So, even though it is not possible to detect a single point at which transition occurs, this model is very useful for purposes of analysis.

In this report, we deal with transition to turbulence in a representative case of shear flow: pipe flow. So, we need to define the Reynolds number for a round cross-section pipe.

$$Re = \frac{UD}{\nu} = \frac{\rho UD}{\mu} \quad (1)$$

where U is the mean velocity, D is the diameter of the pipe, ν is the kinematic viscosity of the fluid, μ is the dynamics viscosity of the fluid and ρ is the fluid density.

In (1), UD represents the inertial term and ν represents the viscous one. Hence, it is clear that for low values of Re , viscous forces are dominant and the fluid flow regularly. When U increases, the inertial term takes over the viscous one and the flow becomes turbulent.

1.3 Dynamics of pipe flow

This report deals with the transition to turbulence of shear flows. However, as mentioned before, we will not discuss about every type of shear flow, but we will focus on pipe flow, probably the most prominent example of shear flux.

Pipe flow, a branch of hydraulics and fluid mechanics, is a type of liquid flow within a closed circular cross-section conduit. The shear flow in a pipe is known as Hagen-Poiseuille flow. In this case, because of the cylindrical geometry, the speed is a function of radius $u(r)$ and in literature [2,3,4] it is considered the case of independence on x (so, it is not given much importance to the length of the pipe).

The fundamental equations that govern the fluid motion, and obviously the pipe flow dynamics, are the Navier-Stokes equations. In Cartesian coordinates x_i the

N-S equations for a not compressible flow with constant properties are written as

$$\frac{\partial u_i}{\partial x_i} = 0 \quad (2)$$

$$\frac{\partial u_i}{\partial t} + u_j \frac{\partial u_i}{\partial x_j} = -\frac{1}{\rho} \frac{\partial p}{\partial x_i} + \nu \frac{\partial^2 u_i}{\partial x_j^2} + f_i \quad (3)$$

If the flow is characterized by high Re , viscous effects and heating ones are confined in small regions (*boundary layers*), resulting negligible in the other parts of the domain. Eliminating these two effects, Navier-Stokes equations can be modified and can be written as

$$\frac{\partial \rho}{\partial t} + \nabla \cdot (\rho \mathbf{V}) = 0 \quad (4)$$

$$\rho \left(\frac{\partial \mathbf{V}}{\partial t} + \nabla \cdot \nabla \mathbf{V} \right) = -\nabla p + \rho \mathbf{f} \quad (5)$$

where ρ is the density, \mathbf{V} is the velocity vector field, \mathbf{f} are the vector field of external forces and p is the pressure gradient.

These equations are known as Euler equations.

Starting from (3), it is possible to obtain the analytical form of the velocity profile in the pipe. We consider a fluid that is: stationary ($\frac{\partial u_i}{\partial t} = 0$), incompressible ($\frac{\partial u_i}{\partial x_i} = 0$) (2) and not subjected to external forces ($f_i = 0$). Furthermore, since $\mathbf{u} = [0, 0, u_z]$, and u_z depends only on r also the term $u_j \frac{\partial u_i}{\partial x_j} = 0$. The velocity profile obtained along the axis is

$$u_z(r) = -\frac{dp}{4\mu dz} (a^2 - r^2) \quad (6)$$

where $a = D/2$ with D the diameter of the pipe and μ is the dynamic viscosity (for more details see ref.[4]). How can be clearly see in (6) and in Fig.1, the velocity profile is a paraboloid: at $r = a$, i.e. on the wall, the velocity is equal to zero. This fact is known as *no-slip condition* which is due to the presence of viscosity; at $r = 0$ the parabolic profile has a maximum, that is the highest velocity in the pipe

$$u_{max} = -\frac{a^2}{4\mu} \frac{dp}{dz}$$

However, the velocity profile depends largely on the Reynolds number (see Section 1.2).

When Re is less than about 30, the Poiseuille theory always provides an accurate description of the flow.

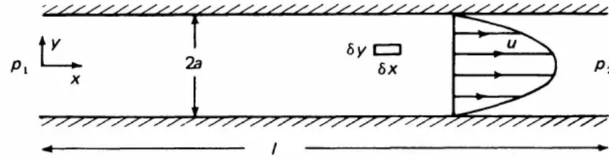


Figure 1: *Definition diagram for pipe flow. It is evident the parabolic shape of the velocity profile obtained in (6). From ref. [4].*

At higher Reynolds numbers, the Hagen-Poiseuille description is no longer valid in all the pipe, but exclusively after some distance down the pipe. At the entrance of the pipe, the flow has not the appropriate parabolic velocity profile, but there is an entry length in which the flow is tending towards the parabolic profile. The higher is the Reynolds number, the longer is this entry zone. The dependence of the extent of the entry length on the Re is $\frac{X}{D} \simeq \frac{Re}{30}$ where X is defined as the distance downstream from the entry at which u_{max} is within 5 per cent of its Poiseuille value.

But, the most dramatic change in flow at higher Reynolds number is the *transition from laminar to turbulent*, of which we will widely discuss in the following chapters. The flow develops a highly random character with rapid irregular fluctuations of velocity in both space and time.

After the transition, many laminar features are not retained. For example, the pressure difference needed to produce a given flow rate through a pipe is larger when the flow is turbulent than when it is laminar (as can be seen in Fig.2).

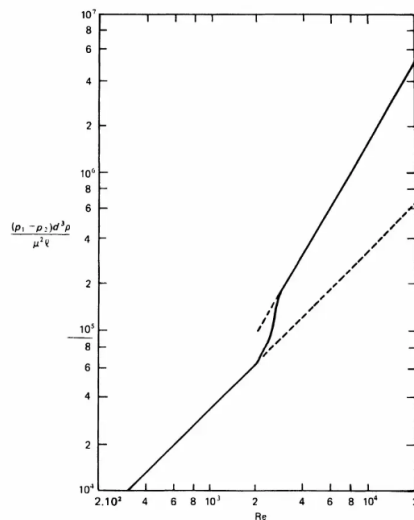


Figure 2: *Variation of non-dimensional average pressure gradient with Reynolds number. Dotted lines represent wholly laminar and turbulent flow. From ref. [4].*

Furthermore, as it is fully explained in Chapter 5, transition to turbulence produce a drastic increasing in friction losses, which are bigger and bigger if the pipe is rough.

The Moody chart (Fig.3) is used qualitatively to study the variation of the friction factor as a function of the Reynolds number and of the relative pipe roughness. It can be divided into two regimes of flow: laminar and turbulent. For the laminar flow regime ($Re < \sim 3000$), roughness has no discernible effect, and the Darcy friction factor f_D , defined in pipe by the Darcy–Weisbach equation:

$$f = \frac{\Delta p}{\frac{\rho U^2 L}{2 D}} \quad (7)$$

(where Δp is the pressure drop over a length L in a pipe with a diameter D and ρ is the fluid density), is determined analytically by Poiseuille law $f = 64/Re$. For a fully turbulent flow and in a smooth pipe the friction factor lies on the Blasius curve $f = 0.3164Re^{-0.25}$. The Blasius equation has no term for pipe roughness and hence it is valid only to smooth pipes (see Fig.3: Smooth Pipe). For rough pipe, Darcy friction factor can be computed thanks to the Colebrook equation that can be solved only by iteration

$$\frac{1}{\sqrt{f}} = -2.0 \log \left(\frac{e/D}{3.7} + \frac{2.51}{Re\sqrt{f}} \right) \quad (8)$$

where e/D is called the relative roughness.

In the chart there is a grey region called *Transition Region*, where happens the switch from laminar to turbulent flow.

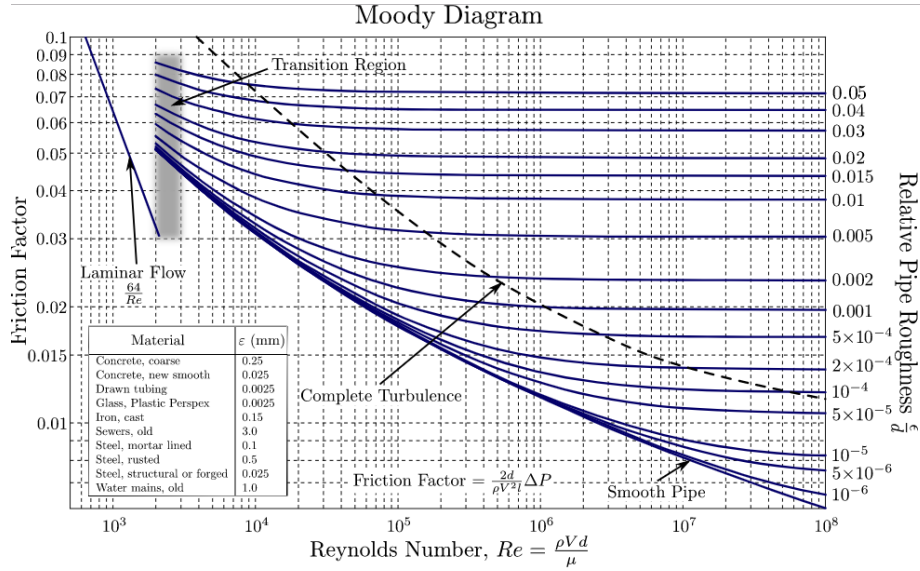


Figure 3: *Moody diagram. This is a graph in non-dimensional form that relates the Darcy friction factor f_D , Reynolds number Re , and surface roughness for fully developed flow in a circular pipe e/D . It is mainly used for qualitative studies. [Original diagram: S Beck and R Collins, University of Sheffield]*

2 Turbulent coherent structures (Birth)

Transition to turbulence in pipe flow is one of the most fundamental and longest-standing problems in fluid dynamics.

The mechanism that leads to the origin of turbulence in wall-bounded shear flows has been studied since the first classical experiments undertaken by Reynolds in 1883, but many aspects still remain to be elucidated.

The transition from laminar to turbulent flow can involve a sequence of instabilities in which the system realizes progressively more complicated states, or it can occur suddenly.

2.1 Puffs, Slugs and Travelling Waves

At moderate flow speeds, turbulence is confined to localized patches; it is only at higher speed that the entire flow becomes turbulent.

Such patches, turbulent structures found in transitional pipe flow, are called *slugs*, if they occur at $Re > 2600$, or *puffs*, if they are observed for $Re < 2600$. The main difference between the two is that *slugs* have a sharp laminar turbulence interface at their leading edge and at their trailing edge; for *puffs* only the trailing interface is sharp.

The process that leads to the formation of these patches (and consequently to the transition) is the so called **lift-up mechanism** [5,6]. Here streamwise vortices of relatively small magnitude transport low momentum fluid away from the wall to the center of the pipe and simultaneously lift high momentum fluid towards the wall, creating local strong anomalies in the velocity profile called *streaks* (elongated regions of low or high streamwise velocity with respect to their surroundings).

If the process was linearly stable, eventually all perturbations would decay.

However, during this process the perturbation amplitude can grow substantially and once it reaches a sufficiently large value nonlinear effects will become important and lead to a secondary instability.

Nonlinear self-interaction of the unstable modes regenerates the streamwise vortices closing the feedback loop, thus sustaining these flow states against viscous decay. [5,6]

This *self-sustained* process has been proposed first by Hamilton *et al* and Waleffe [7,8].

This nonlinear nature of fluid turbulence has suggested to focus on the nonlinear solutions to the fundamental equations of Navier-Stokes.

In pipe flow, the simplest of these solutions are **travelling waves (TWs)**, which

provide a dynamical and fully nonlinear approach to the problem.

TWs are defined as *exact coherent structures* (Waleffe 1998, 2001, 2003), because they share with coherent structure the presence of some large-scale features, a predictable dynamics, and a relatively frequent occurrence and they are exact solutions to the equation of motion.

These solutions satisfy

$$\mathbf{v}(x, r, \theta, t) = \mathbf{v}(x - ct, r, \theta) \quad (9)$$

where (x, r, θ) are cylindrical coordinates, t time and c the wave speed, that is constant in streamwise direction.

Confirmation of this picture has been provided by several experiments in pipe flow. Surprisingly clear transients of travelling waves were observed confirming their relevance to the turbulent dynamics. Furthermore, transients of unstable TWs have been observed that are in close agreement with numerical solutions.

2.2 Setup of experiments

The first experimental observations of the transition from laminar to turbulent in pipe flow was undertaken early in 1880 by Osborne Reynolds. In his 1883 paper [1] Reynolds described the transition from laminar to turbulent flow in a classic experiment in which he examined the behaviour of water flow under different flow velocities using [...] *three tubes, whose diameters were nearly 1-inch, $\frac{1}{2}$ -inch, and $\frac{1}{4}$ -inch. They were all about 4 feet 6 inches long, and fitted with trumpet mouthpieces, so that water might enter without disturbance. The water was drawn through the tubes out of a large glass tank in which the tubes were immersed, arrangements being made so that a streak or streaks of highly coloured water entered the tubes with the clear water.*

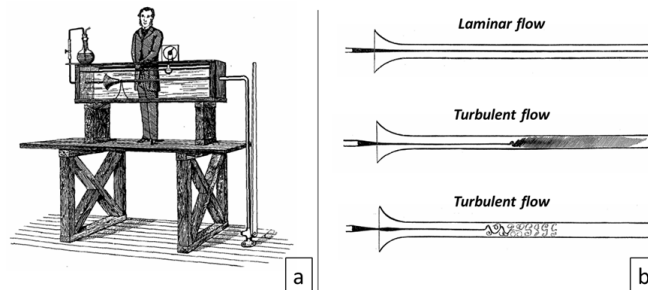


Figure 4: *Osborne Reynolds's apparatus of 1883 demonstrating the onset of turbulent flow. The apparatus is still at the University of Manchester.*

After this pioneering experiment, many efforts have been made in order to

increase the quality of the observations and obtain the most satisfactory results, thanks to many devices installed on the pipe used for the experiments.

In the Appendix we provide a detailed description of the experimental setup used by Hof *et al.* in 2004 [5]. We have chosen to describe only one of the numerous experimental apparatuses used in the last years as they follow indicatively the same scheme.

The experimental procedure is to create a single turbulent puff close to the pipe inlet and to monitor any changes in the turbulent fraction at downstream position.

In pipe flow laminar profile is linearly stable for all Reynolds numbers. Thus, to trigger transition, two thresholds have to be crossed: the flow has to be sufficiently fast and a perturbation has to be strong enough. In modern times, taking extraordinary care and minimizing inlet disturbances enable laminar flow to be maintained to higher flow rates (Reynolds number of $\simeq 100000$).

Hence, it is important to choose efficiently a perturbation capable of triggering turbulence. Darbyshire & Mullin (1995) [10] established the possibility of systematic dependence of the threshold amplitude for disturbances added to fully developed flow. However, a scaling could not be extracted from their results and it was Hof *et al.* (2003) [9] who showed that the threshold amplitude ϵ (defined by the volume flux Φ_{inj} from the injector) of a jet disturbance has a scaling of $\epsilon = O(Re^{-1})$ over a significant range.

In Fig.5a stability curves for two different values of Re are shown. The amplitude of perturbation required to cause transition is plotted as a function of length* (that is an estimation of the spatial extent of the disturbed flow immediately downstream of the injection point).

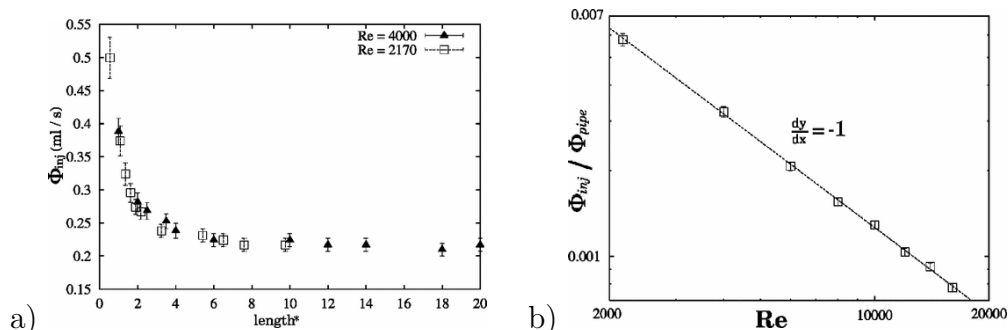


Figure 5: a) Stability curves measured for $Re = 2170$ and $Re = 4000$. Error bars correspond to the widths of the determined probability distribution after 40 runs of experiment. b) A log-log plot of the stability curve obtained using the long pipe. The range of Re covered is 2000 to 18 000 and the amplitude of perturbation has been nondimensionalized by the respective mass flux in the pipe. From ref. [9]

Perturbations with amplitudes below the curve did not cause transition and decayed as they propagate downstream. On the other hand, for disturbances above the threshold, transition takes place and the state achieved is either a puff or slug depending on Re . Each data point was obtained by repeating the experiment around 40 times since the threshold is a statistical process as discussed by Darbyshire & Mullin (1995) [10].

From Fig.5b it is clear the proportionality between the amplitude of the perturbation and the Reynolds number, also for high Re values. Here we can see that the threshold data are not represented below $Re = 2000$ since experimental evidence suggests that turbulent flow cannot be maintained below this value.

2.3 Experimental and numerical results

Several experiments have been carried out in order to study this phenomenon. The introduction of PIV measurements has enabled to determine and visualize the in-plane and the out-of-plane velocity field, so that the full three component velocity field in the measurement plane was obtained.

Three velocity fields in the cross-sectional plane measured during the passage of the turbulent slug (or puff) are shown in Fig.6, where experimentally (top) and numerically (bottom) observed streak patterns are compared. Regions of high velocity relative to the laminar profile are shown in red, regions of low velocity relative to the laminar profile are shown in blue, and transverse components are indicated by arrows.

In these pictures, firstly we can see how, regardless of Reynolds number, the turbulent flow is composed by two main highly symmetric regions with two different behaviours: the central region where low-speed streak is found and the near-wall region where we can observe high-speed streaks. Another characteristic that can be observed is that the section of each high-speed streak has roughly the same elliptical shape, they are well-ordered azimuthally along the wall but their number changes; low-speed streak is characterized by a core from which a varying number of arms departs. The number of these streaks and arms depends on Re . Depending on the Reynolds number considered, each experimentally observed streak pattern corresponds to a C_m symmetric traveling wave, where the subscript m specifies an m -fold rotation symmetry (confirming the presence of travelling waves solutions) [11].

Furthermore, as explained in the previous sections, the self-sustained process implies the existence of several pair of vortices that are responsible of the creation of the streaks. Also the number of these eddies depends on Re : three and two

vortex pairs were observed in turbulent puffs at $Re = 2000$ (**A**) and $Re = 2500$ (**C**) and coherent states with four and six vortex pairs were observed in fully developed turbulence at $Re = 3000$ and $Re = 5300$ (**E**).

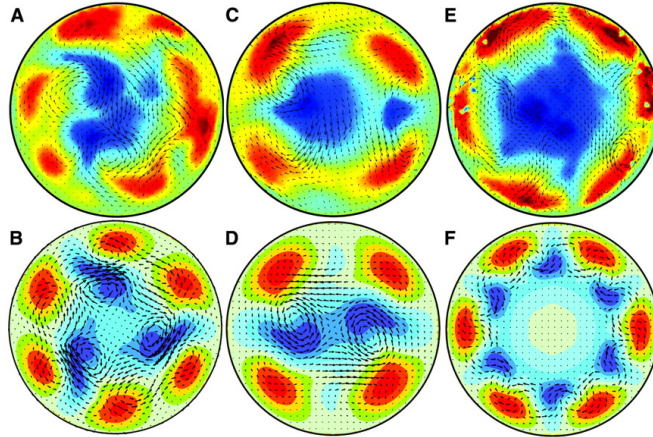


Figure 6: *Comparison of experimentally (top) and numerically (bottom) observed streak patterns. Here the laminar flow profile is subtracted from the measured downstream velocity components. The color coding for the experimental flow patterns ranges from plus (dark red) to minus (dark blue) $0.6U$; the numerical flows range from plus (dark red) to minus (dark blue) $0.4U$. From ref. [5].*

Comparing these streak configurations with the numerical ones, the arrangements of high- and low- speed streaks of these states closely resemble those of the travelling waves.

Until now, we have compared the static streaks configuration as seen in cross-sectional plane at a determined moment.

What about the time evolution of the turbulent pattern?

The four cross section shown in Fig.7 are separated by 0.2s, which, based on the bulk flow speed, correspond to a spacing of 0.18 pipe diameters. In this case the travelling wave transient has been observed in a turbulent slug at $Re = 3000$. The general configuration is similar to that of Fig.6, indeed we can find the high-speed streaks near the wall (shown in red) and the low-speed streak in the center (shown in blue). In particular, this wave transient showed a C_4 symmetric configuration. Two distinct low-speed streak arms are distinguishable, which initially point outwards from the pipe center in the horizontal direction. They subsequently undergo an anti-symmetric up and down motion while high-speed streaks essentially remain in the same position.

This dynamical behaviour is in excellent qualitative agreement with that reported for the numerically observed TWs.

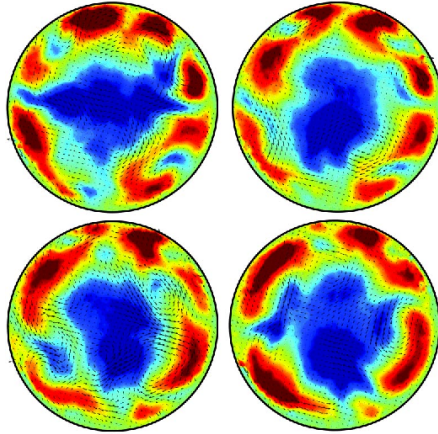


Figure 7: *Travelling wave transient observed in a turbulent slug at $Re=3000$. Instead of subtracting the laminar profile from the streamwise component as in Fig.6, Hof et al. have chosen to subtract $0.5LP + 0.5 TP$. Thanks to this visualization method the streaks in the near wall region are resolved more clearly. From ref. [6].*

Finally, the time spacing of the measurements can be converted into a spatial separation in the mean flow direction (Taylor’s hypothesis¹) allowing full spatial 3D reconstruction of the turbulent structure.

The rotational symmetry of the streak structure and the periodic modulation of the low-speed structure corresponding to the up and down motion can be clearly seen in Fig.8. A further evidence of the self-sustained process (of which we spoke about above) comes from the picture on the right. In this three-dimensional reconstruction, the same low-speed streak of a) (blue) is displayed together with the two counter-rotating streamwise vortices (yellow and red). These vortices are responsible of the lift-up process that generates the turbulent patches.

How we can see, a second pair of streamwise vortices surrounds the streak downstream. These vortices are generated due to the wavy instability of the streak. The periodicity of the eddies confirms the existence of the self-sustained process and the nonlinearity of the transition mechanism.

The most characteristic feature of these travelling wave solutions, i.e. the wavelength, has been estimated by Hof, Van Doorne et al. (2005) [6] thanks to these 3D reconstructions. The second pair of vortices aligns the streak approximately $0.7D$ (where D is the diameter of the pipe) further downstream, thus the wavelength of the TW has been estimated to $\simeq 0.75D$.

¹**Taylor’s frozen flow assumption:** advection contributed by turbulent itself is small and therefore the advection of a field of turbulence past a fixed point can be taken to be entirely due to the mean flow; it only holds if the relative turbulent intensity is small, i.e. $\frac{\bar{u}}{U} \ll 1$ where \bar{u} is the eddy velocity and U is the mean flow velocity. Then the substitution $t = x/U$ is a good approximation

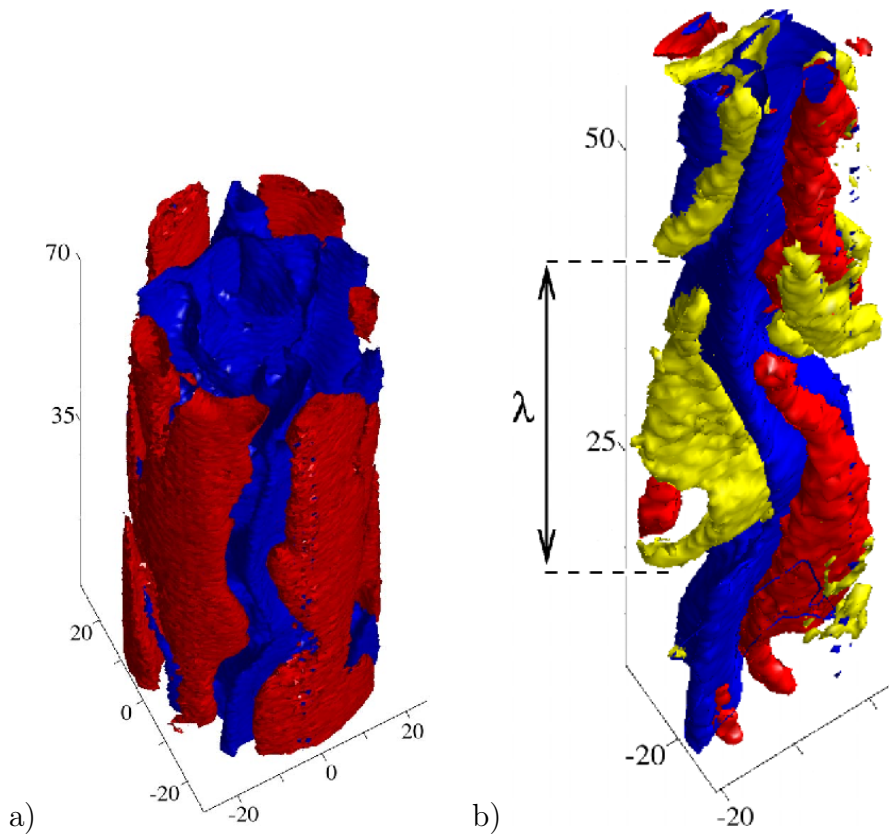


Figure 8: In both pictures, length units are in millimeters. a) Reconstruction of the three-dimensional streak structure of the traveling wave. High speed streaks are shown in red and low speed streak is shown in blue. The blue low-speed streak undergoes a wavy instability (as we will see better in Chapter 5). b) Three-dimensional reconstruction of the wavy low-speed streak and the streamwise vorticity. Positive and negative vorticity is shown in yellow and red. The wavy low-speed streak (shown in blue) is sandwiched between the counter-rotating streamwise eddies. In the picture is highlighted the wavelength λ that is measured from the upstream front of the first vortex and the upstream front of the new vortex seeded downstream. From ref. [6].

3 Turbulent fronts propagation (Growth)

In Chapter 2, the concepts of puff, slug and travelling wave were introduced and it has been explained their structure, their function and the mechanism that generates them.

Here, it will be described how they propagate and eventually succeed in triggering sustained turbulence .

The process that allows turbulent puffs to propagate depends mainly on the Reynolds number. Indeed, starting from a single puff, turbulence proliferates through a sequence of splittings at $Re = 2300$ (Fig.9 **A**). For $Re \leq 2300$ spreading of turbulence and hence any increase in turbulent fraction was exclusively observed in the form of puff splitting. Only at Reynolds numbers bigger than 2400 (Fig.9 **B**) do individual puffs start to noticeably expand so that the overall spreading of turbulence becomes a complex mixture of splitting, as well as growth and merging of individual turbulent domains. Finally, if $Re \leq 2040$ puff is destined to decay before succeed in splitting or growing, and thanks to that, spreading turbulence [12,13,14].

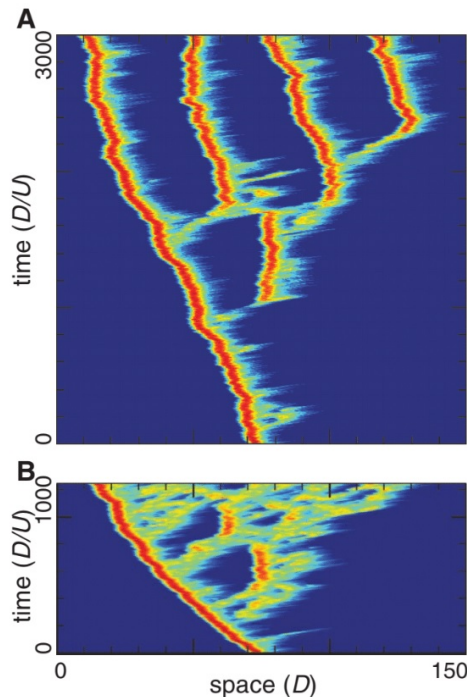


Figure 9: *Spreading of turbulence in numerical simulation. (A) $Re = 2300$, where the expansion process is dominated by discrete steps, corresponding to puff splits, whereas (B) $Re = 2450$, where expansion is more smooth, more rapid, and individual puffs are no longer easily identified. From ref. [12].*

Hence, we can think to divide the mechanism that leads to the spreading of the turbulence in two different processes: **puff splitting** and **slug spreading**.

3.1 Puff splitting ($Re \leq 2300$)

At low Reynolds numbers, turbulence is localised in the form of puffs surrounded by laminar flow and the upstream and downstream front speeds are identical. This velocity is lower than the mean flow speed and so, in the reference system relative to the bulk velocity of turbulence, the localized puff moves backwards. As said previously, puffs are characterized by a sharp trailing laminar turbulence interface and a rough leading edge.

In the picture below (and also in Fig.9A) we can clearly see the difference between the upstream front (shown in black) and the downstream front (shown in yellow). Furthermore, it can be observed that the two fronts propagate at the same speed, since the puff has always the same length with increasing time.

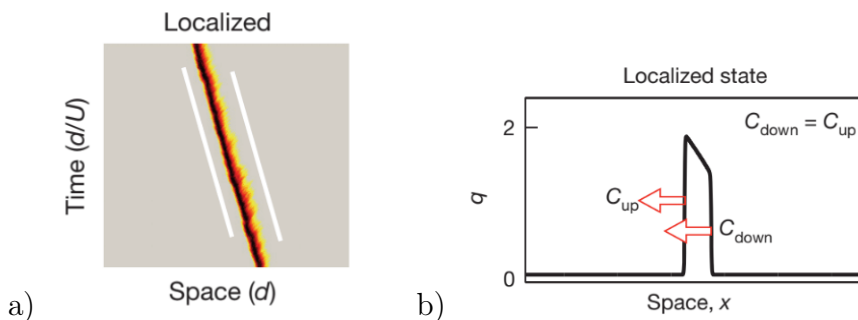


Figure 10: a) Space-time plot from simulations of pipe flow at $Re = 2000$. Here it is clear that turbulence is localized with equal upstream and downstream front speed. b) Localized state predicted by the model proposed in ref. [13] at $Re \simeq 2000$. The state is plotted in the local phase plane, where q denotes the turbulence level within the flow and x is the space along the pipe axis. C_{up} (the upstream velocity) is equal to C_{down} (the downstream velocity), yielding localized turbulence. From ref. [13].

The configuration shown in Fig.10 corresponds to the first part of the graph² ($Re < 2300 - 2400$) in Fig.11 where front speed as a function of Reynolds number for pipe flow is displayed. As we can see both front speeds, downstream and upstream, coincide and they decrease with increasing Re .

In Fig.11 points are experimental results taken from the literature as indicated and the continuous blue curve comes from model predictions by Barkley et al (for more detail check ref. [13]).

As already mentioned, after triggering disturbance, puffs can decay, or else split and thereby multiply. For $Re > 2040$, the splitting process outweighs decay, resulting in sustained disordered motion.

²The second part of the graph will be considered in the following section.

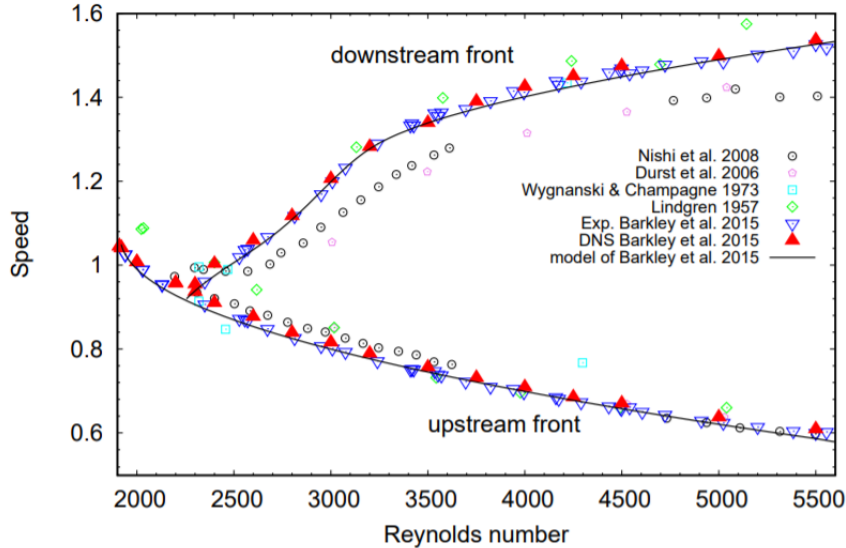


Figure 11: *Front speeds as a function of Reynolds number for pipe flow. Points are experimental results taken from the literature as indicated. The black curve comes from the model of Barkley et al. 2015. This graph can be used as a guide to establish the behaviour of the fluid at a determined Reynolds number. From ref. [14].*

Because of the stochastic nature of the splitting process, a statistical approach must be used.

K. Avila et al. (2011) [12] found out that the probability of puff splitting $P(Re, t)$ (plotted in Fig.12) is exponential and hence memoryless, reflecting that the probability of splitting does not depend on the age of the puff observed. Thanks to numerical simulations and long-pipe experiments, they were able to write the probability distribution as

$$1 - P(Re, t) = \exp\left(-\frac{(t - t_0)}{\tau(Re)}\right) \quad (10)$$

where t is the observation time, t_0 is the formation time which includes any equilibration time for the initial conditions to evolve to the turbulence state at the particular Re and the intrinsic time needed for splitting. It depends on Re , but is found to be consistently $\in [100, 200]$. Finally, $\tau(Re)$ is the Re -dependent characteristic time for the process that decreases with the Reynolds number, unlike the time scale that characterize the decay of puffs which increases rapidly with Re^3 .

The behaviour of the two above mentioned characteristic timescales is displayed in Fig.13. Data from both experiment and direct numerical simulation (DNS) are shown. The decay data on the left branch is primarily taken from past studies³.

³In the next chapter we will talk about lifetime and decay of puffs.

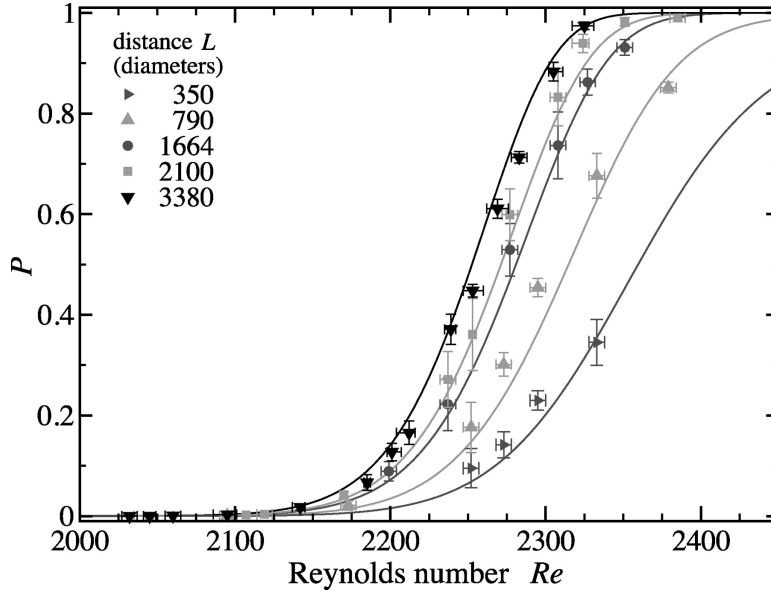


Figure 12: Probability of puff splitting after travelling a fixed distance. The five data sets correspond to distances L in the experiments of K. Avila et al. [12], as indicated in the legend. The error bars in the vertical direction are 95% confidence intervals for the parameter P , whereas in the horizontal direction they show the uncertainty in Re during a set of measurements. The solid line correspond to the superexponential fit explained in the Chapter. From ref. [12].

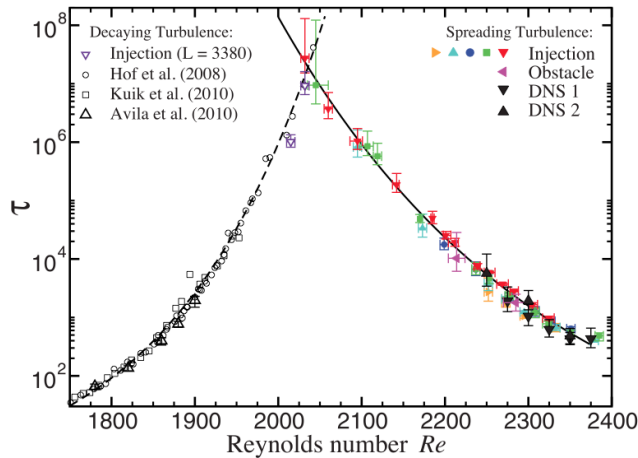


Figure 13: Mean lifetime of a puff before decaying or splitting. Solid colored symbols correspond to experimental splitting measurements. The solid black triangles show the characteristic splitting time obtained from direct numerical simulations using the spectral-element Fourier code (DNS1) and the hybrid spectral finite difference code (DNS2). The solid curve is given by $\tau = \exp[\exp(-0.003115Re + 9.161)]$ and approximates the Re -dependence of mean time until a second puff is nucleated and the turbulent fraction increases; the dashed curve is given by $\tau = \exp[\exp(0.005556Re - 8.499)]$ and approximates the Re -dependence of the mean time until turbulence decays and the flow relaminarizes. Both curves correspond to superexponential scaling with Re and have a crossover at $Re = 2040 \pm 10$, determining the transition between transient and sustained turbulence in pipe flow in the thermodynamic limit. From ref. [12].

The intersection at $Re = 2040 \pm 10$ marks where the mean lifetime is equal to the mean splitting time, and after this point, splitting outweighs the decay of puffs. This crossover determines the transition between transient and sustained turbulence in pipe flow.

Although typically in statistical phase transition, critical points are not identical to the exact balance point of two competing processes because of correlations, in the present case the superexponential scaling of the two processes ensures that the critical point will be almost indistinguishable from the intersection point.

Finally, also from these data it is clear that before $Re \simeq 2040$ a puff is not strong enough to split (due to τ very high) and so a larger cluster of turbulence cannot form.

3.2 Slug spreading ($Re > 2400$)

At higher Reynolds numbers, turbulence begin to expand in streamwise extent and eventually render the flow fully turbulent. Such expanding turbulent regions are known as slugs. As said previously, slugs are characterized by both sharp trailing and leading laminar turbulent interface.

However, it is necessary to make a further distinction since the downstream spreading exhibits a more complex behaviour observed just recently. At moderate Reynolds numbers, slugs have diffusive downstream fronts, not unlike the downstream fronts observed for puffs (see Fig.14 **Weak**), whereas at high Reynolds numbers the downstream fronts are sharper, with a well-defined structure similar in intensity to the upstream fronts (see Fig.14 **Strong**). Barkley et al. (2015) [13] referred to the diffusive form of the downstream fronts as weak fronts and the sharper form as strong fronts. The corresponding slugs are thereby called weak and strong slugs, respectively.

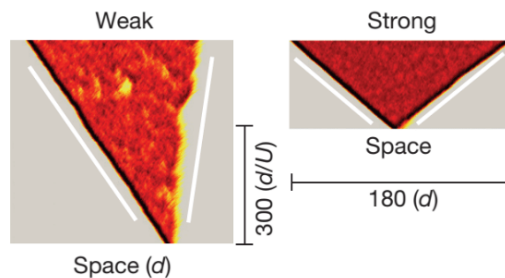


Figure 14: *Space-time plots from simulations of pipe flow at $Re = 2800$ (left) and $Re = 4500$ (right). At $Re = 2800$, the downstream front moves at a speed between the weak and strong branches and exhibits some characteristics of both fronts as it fluctuates. At $Re = 4500$, turbulence expands with a strong downstream front and the long-time flow is fully turbulent. The upstream and downstream front have the same character. From ref. [13]*

The two cases illustrated in the figures above correspond to the second part of the graph in Fig.11. After the first part where upstream and downstream coincide, expansion begins with the formation of the *weak* downstream front. Weak downstream front moves slowly than the bulk advection velocity of turbulence and so, how can be seen in Fig.15 both fronts continue to move backwards with respect the moving frame of reference with the mean velocity of the flow. However, since C_{down} (speed of the downstream edge) is different from C_{up} (speed of the upstream edge), slug starts expanding. This state persists until the downstream front speed exceeds the bulk advection velocity.

At this point, approximately at $Re = 2800$, a type of switching between weak and strong downstream fronts has been frequently observed. For $2800 < Re < 3200$,

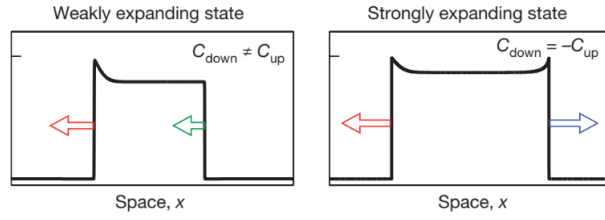


Figure 15: The two represented states are plotted in the local phase plane, where q denotes the turbulence level within the flow and x is the space along the pipe axis. (left) Weakly expanding state predicted by the model proposed in ref. [13]. The system presents a strong front (upstream, speed indicated with the red arrow) and a weak front (downstream, speed indicated with the green arrow). $C_{down} \neq C_{up}$, but they move in the same direction. (right) Strongly expanding state predicted by the model proposed in ref. [13]. The downstream and the upstream fronts have the same character, but move in opposite directions, $C_{down} = -C_{up}$ (respectively, the blue and the red arrow), in a reference frame moving at the neutral speed. From ref. [13].

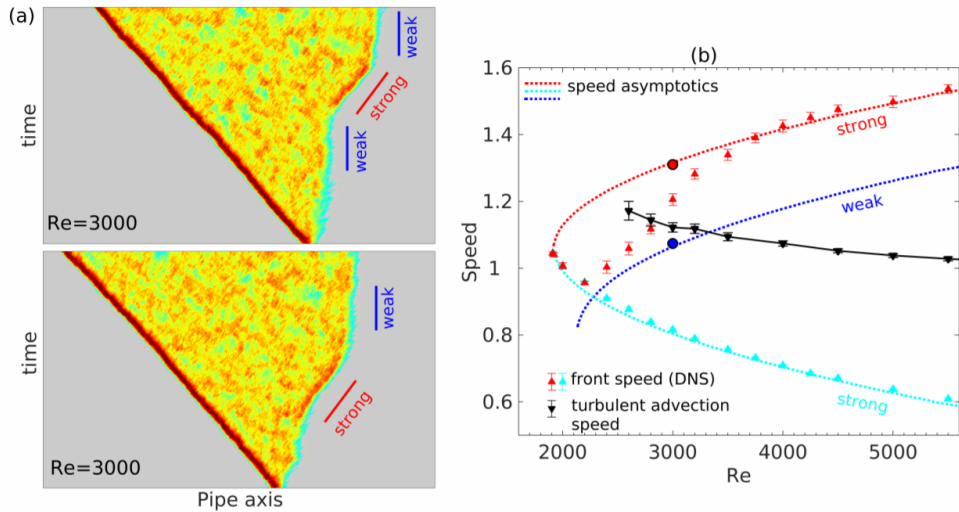


Figure 16: Switching between weak and strong front at $Re = 3000$. a) Space-time diagrams showing the colourmap of q for two typical slugs in a moving frame of reference with the speed of $1.06U$ (the speed of the weak front at this Reynolds number). The bars show the slopes, i.e. the inverse of the speeds, of transient weak and strong fronts in this frame of reference. b) Front speed as a function of Reynolds number from DNS (up-triangles) and from an asymptotic analysis of fronts in a model system (dotted lines), reproduced from Barkley et al. (2015). From ref. [14]

the expanding state passes through a transition zone that originates downstream front fluctuations (see Fig. 16b). Here the front speed switches from the weak to the strong speed asymptotics (predicted by the theory of Barkley *et al.* (2015) [13]).

On the other hand, after bifurcation, upstream laminar turbulent interface does not change at all. Its speed carry on following the behaviour described by the lower branch in Fig.11.

In this region, turbulence is not always uniform, but commonly contains intermittent laminar pockets.

Finally, when the downstream speed reaches the strong speed asymptotics, the turbulent patch invades fully recovered laminar flow at the downstream front, in much the same way that turbulence invades fully recovered laminar flow at the upstream front. This produces a slug that aggressively expands and eliminates all laminar motion. The downstream speed increases until it becomes equal (in modulus), but opposite in direction to the upstream speed (see the schematic picture on the right in Fig.15) and this produces the symmetry between the upstream and strong downstream fronts.

3.3 Energy budget at the fronts

Wyganski & Champagne (1973) [16] analysed the turbulent kinetic energy of their experimental data, focusing on the radial distribution and the balance of all components of the energy budget. In 2017, B.Song *et al.* [14] revisited Wyganski & Champagne's turbulent kinetic energy budget in order to shed light on the origin of the different turbulent intensity profiles at weak and strong fronts.

In order to do this, they have studied the equation for the mean kinetic energy of the turbulent fluctuations in the formulation of Pope (2000) [17] using Reynolds decomposition of the velocity field. The main discrepancy was found about the order of magnitude of production and dissipation. These two are the source and sink terms in the energy budget and Song's calculation shows that they are comparable in magnitude at all axial positions. In their work Wyganski & Champagne (1973) reported that dissipation is orders of magnitude smaller than production at the fronts.

In Fig.17 are displayed the cross-sectionally integrated energy budget for turbulent fronts at $Re = 2600$ (a, b) and $Re = 5000$ (c, d). How we have already widely explained, at $Re = 2600$ slug presents a strong upstream interface and a weak downstream edge, whereas at $Re = 5000$ turbulent flow is fully turbulent and both upstream and downstream fronts are strong. So, if we focus on the strong edges (a, c, d), as one looks into the fronts from the laminar side (i.e.

from the left for UF and from the right for DF), turbulence production (red line) first increases sharply, whereas the increase in dissipation (blue dash-dotted line) is significantly delayed with respect to the production. This is a clear indication that there are large eddies at the strong fronts extracting energy from the adjacent laminar flow.

As one moves further towards the bulk, the energy production rate decreases and

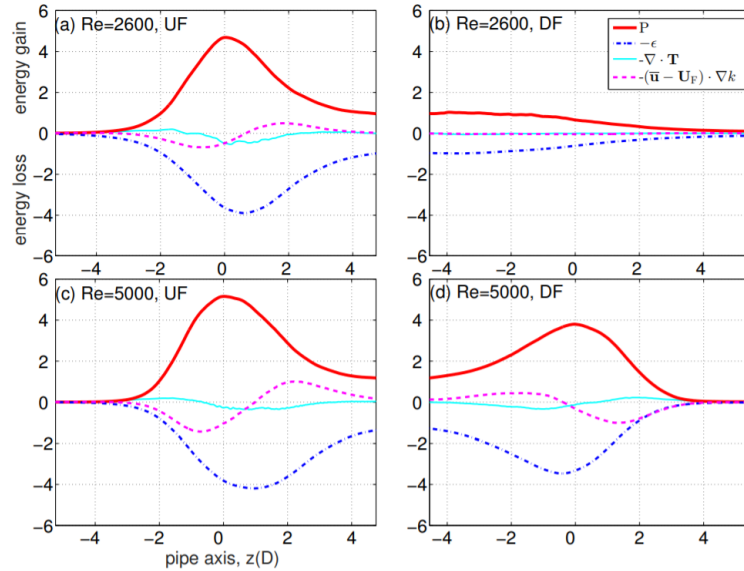


Figure 17: *Kinetic energy budget (integrated over pipe cross-section) in the frame of reference co-moving with the fronts. Production (red bold line), dissipation (blue dash-dotted line), energy flux (cyan thin line), and convection (violet dashed line)*

dissipation outweighs production. As a result the turbulence intensity decreases and the strong front eventually manifests an intensity peak.

At weak fronts no significant delay of dissipation with respect to production can be observed. Here energy production and dissipation balance each other over any cross-section (see Fig.17b), and there is no significant transport of energy along the streamwise direction. This implies that in weak front turbulence is locally in equilibrium, which results in the absence of peak in the turbulence intensity.

The presence or the absence of peaks is also sketched in Fig.15 where the strong edge is represented with a peak unlike the weak edge.

4 Turbulent lifetime (Death)

In the previous chapters, it has been explained how turbulent patches rise, what their structure is and how they spread, thereby generating a sustained turbulence. Now, in this chapter, we are going to address an important issue, useful to understand which could be the destiny of turbulence propagation: **turbulence lifetime**.

It is defined as the time when the energy content in the perturbation drop below a level from which it cannot recover, so that one has entered in the *basin of attraction* of the laminar profile.

Basin of attraction is one of the main concept included in the **dynamical system theory**. In the past few years it has emerged that this theory can be fundamental for the understanding of the properties of transition pipe flow.

4.1 Introduction to dynamical system theory

In this small section we explain some concepts from the dynamical system theory that have been really helpful to better figure out turbulence mechanisms.

A dynamical system consists of an abstract *phase space* (or *state space*), whose coordinates describe the state at any instant, and a dynamical rule that specifies the immediate future of all state variables, given only the present values of those same state variables. In our case, the state space should provide a complete description of the dynamics, in that at any point in this space the Navier-Stokes equations together with boundary conditions uniquely determine the evolution. In our phase space, there is one region dominated by laminar flow. Initially, below the formation of the turbulent structures, laminar state is a, so called, *attractor*. Roughly speaking, an attractor for a dynamical system is a closed subset \mathbf{A} of its phase space such that for "many" choices of initial point the system will evolve towards \mathbf{A} . The union of all orbits which converge towards the attractor is called the basin of attraction $\mathbf{B}(\mathbf{A})$ [18]. This means that all initial conditions return to the laminar profile indicated by the blue circle (see Fig.18a).

The turbulent dynamics take place in other parts of the state space (see red point in Fig.18b). Initially, the turbulent state is a chaotic *repellor* in phase space, which gives rise to long-lived turbulent transients. The phase-space dynamics of turbulence is organized around travelling waves (see Section 2.1) that are unstable numerical solutions of the Navier-Stokes equations. As one approaches the critical point for the onset of the structure, one initial condition is slowed down and ends up in the critical point, indicated in red. As the Re increases, the laminar state is still stable, but it is reduced from a global to a local attractor; the basin of the turbulent state grows, whereas that of the laminar one diminishes in

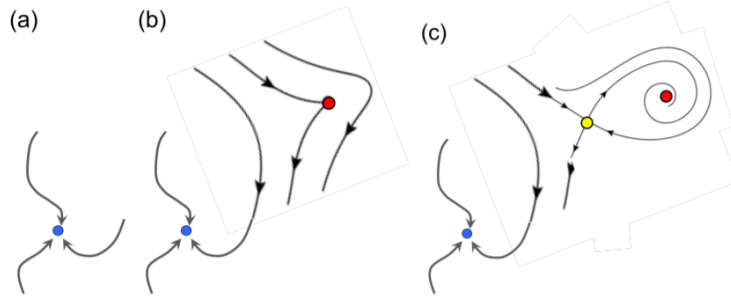


Figure 18: A sketch of the saddle-node bifurcation in the state-space of the system. a) Below the appearance of exact coherent structures, all initial conditions return to the laminar profile (blue dot), as indicated by the arrows. b) At the critical point, one set of initial conditions converges to the new exact coherent structure (red dot). c) Above the critical point a saddle (yellow) and a node (red) appear and a finite regions of initial conditions is attracted to the node. From ref. [19].

proportion to Re^{-1} (i.e. the number of initial conditions that lead to turbulent flow markedly increases). Consequently, as pointed out in Section 2.2, smaller and smaller perturbations to the laminar flow are sufficient to cause a transition to turbulence.

This scenario may suggest that, at high Reynolds numbers, turbulent repeller evolves into a turbulent attractor. However, as it is explained later in the Chapter, the possibility of decay indicates that the basin of attraction of turbulence is not compact nor space filling; there must be connection to the laminar profile. In dynamical systems such structures are known as *chaotic saddles* or *strange saddles*: with chaotic attractors⁴ they share positive Lyapunov exponents⁵ for the motion close to the saddle, but they are not persistent and have a constant probability of decay [11].

Hence, above the critical point, a saddle point (yellow) and a node (in red) appear and a finite regions of initial conditions is attracted to the node (Fig.18c). The saddle point has stable and unstable directions, with the unstable directions either pointing towards the laminar profile or to the new node. In the example shown in (c), the saddle has one unstable direction, and the node has only stable directions.

Another analogy to help one visualize the meaning of a chaotic saddle is that of a particle in a box with curved walls (Ott E. 1993 [20]). The particle dynamics

⁴**Chaotic attractor**: exhibits sensitive dependence on initial conditions: any two arbitrarily close alternative initial points on the attractor, after any of various numbers of iterations, will lead to points that are arbitrarily far apart, and after any of various other numbers of iterations will lead to points that are arbitrarily close together.

⁵**Lyapunov exponent** (λ): it gives a measurement of the sensibility of the dynamical system orbits for the initial conditions. If $\lambda > 0$: great dependence on the initial conditions. Furthermore, it can be defined a characteristic timescale as $\frac{1}{\lambda}$ that mirrors the limits of the predictability of the system.

is such that the particle moves along straight lines until it hits a wall where it is elastically reflected. With the exception of a spherical, ellipsoidal, or rectangular shape, nearly any boundary will produce chaotic particle dynamics. The fact that this model is energy conserving whereas a hydrodynamic flow is dissipative should not be of concern: If the dynamics is expanded to include friction on the particle and a motor that keeps the particle in motion, one arrives at a dissipative analog with the same key features. To obtain a chaotic saddle, introduce a hole into the wall through which the particle can escape. Until the particle hits the hole it will bounce around chaotically, and the dynamics will have a positive Lyapunov exponent λ . Because of the positive Lyapunov exponent, correlations in trajectories will disappear quickly (on a timescale of the order of $\frac{1}{\lambda}$), and the probability of hitting the escape hole remains nearly the same: whenever the particle hits the wall it escapes with a probability equal to the area of the hole divided by the total surface area.

4.2 Distribution of lifetimes

Two implications of strange saddle that can be observed in pipe and other shear flow are: a) the distribution of lifetimes becomes exponential for long times, b) the decay of turbulence at some point in time without any noticeable prior indication. These two observations are obviously connected. If the probability of decay is constant in time and independent of when the turbulence was started (b), then this means that the distribution of lifetimes is exponential (or better, *super-exponential*) (a).

Initially, it was generally assumed that, once the transition has taken place, under steady conditions, the turbulent state will have persisted indefinitely and it was thought that the lifetime would diverge at some critical Reynolds number. However, extensive calculations and experimental studies have shown that turbulence in pipes is transient, and that the lifetime increases *super-exponentially* with Re [21,22,23].

The *super-exponential* behaviour of the lifetime was firstly discovered by Hof et al. (2008) [22], who repeated the experimental studies carried out in the previous years (see Appendix) with substantial technical improvements. In their work in 2008, Hof et al. identified two main constraints needed to be improved: first of all the limited range in lifetimes measured that causes insufficiently resolved statistics and secondly the initial formation time t_0 that can be larger than the actual observation time and this causes significant uncertainties in the evaluations of lifetimes.

The implementation of accurate temperature control allowed measurements to

be carried out at constant temperatures ($\pm 0.05K$) for several days and hence avoiding Reynolds number changes caused by the temperature dependence of the viscosity. Furthermore, the pipe section was accurately aligned and special care has been taken at the pipe inlet to avoid turbulence being induced. The automation of the measurement techniques combined with these improvements allow them to prolong the observational time-span up to 8 orders of magnitude.

In Section 3.1, we have introduced a probability function $P(Re, t)$ that is the probability of pluff splitting after a time t .

Likewise, we can define the probability [21] for a flow to still be turbulent after a time t at a fixed Reynolds number (Re) as

$$\bar{P}(Re, t) = \exp \frac{-(t - \bar{t}_0)}{\bar{\tau}(Re)} \quad (11)$$

where $\bar{\tau}$ is the characteristic lifetime ($k = \bar{\tau}^{-1}$ can be also interpreted as the escape rate) and \bar{t}_0 is the initial time period required for the turbulence to form after the disturbance has been applied to the laminar flow at $t = 0$ ($\bar{t}_0 \ll \bar{\tau}$).

The superposed bar highlights the difference between quantities in (3) and (4) and from henceforth we omit it.

The very rapid increase of $\tau(Re)$ with Re reported in earlier studies led to the conclusion that τ diverges at some finite Reynolds number Re_{crit} , that is $\tau(Re) \propto 1/(Re_{crit} - Re)$. Using this theoretical definition of τ , we would expect that $P(t, Re)$ (4) increases exponentially with Re , that the steepness of the exponential increases with t and that independent of the value of t all curves reach $P = 1$ at Re_{crit} . (see the dotted curves in Fig.19).

This theoretical model proposed by Faisst & Eckhardt in 2004 [24] was re-considered in view of experimental and numerical results obtained in more recent studies. Indeed, τ^{-1} has been observed to decay exponentially and not linearly (reaching zero at the critical Reynolds number)! Crucially it only approaches zero and hence an infinite lifetime is only reached in the asymptotic limit $Re \rightarrow \infty$. The probability distributions are S shaped and not simple exponentials as would be expected if $\tau(Re)$ was a linear function. The observed distributions are not self-similar (as suggested by Hof *et al.* in 2006) but instead their maximum slope (at $P(t) = 0.5$) increases with L/D , where L is the length of the pipe and D is the diameter.

For each of the measured probabilities $P(t)$ inverse characteristic lifetime $\tau^{-1}(Re)$ can be determined using (11). In Fig.20 are shown the escape rates and confidence intervals given by the studies of Peixinho & Mullin 2006 (black stars), Hof *et al.* 2006 (crosses), Willis & Kerswell 2007 (rhombuses), Hof *et al.* 2008 (squares)

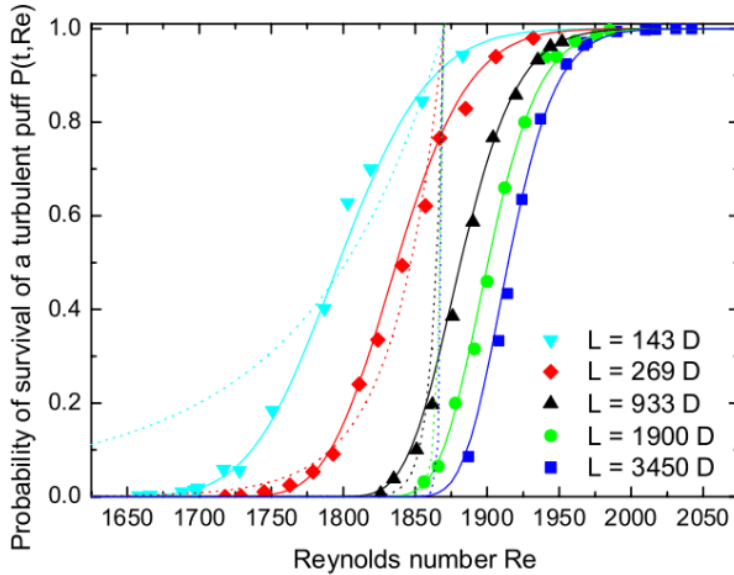


Figure 19: Probabilities for the flow to still be turbulent after travelling a fixed distance x . The fitted curves follow directly from the superexponential scaling shown in Fig.20. The dotted curves show the scaling that would be expected for the critical behaviour suggested by Willis and Kerswell [26]. From ref. [22].

[25,21,26,22] and finally the data obtained by Avila *et al.* in 2009 (black circles) [23]. As said previously, the experiment carried out by Hof *et al.* in 2008 can be considered the most accurate one, and so we can use their results as points of reference. The agreement with the simulations of Willis & Kerswell (2007) [26] is very good between $Re = 1740$ and $Re = 1820$ even if τ is considered to be linear. For $Re < 1720$ (before the vertical dash-dotted line) no evidence of exponential behaviour in the lifetimes has been found. It is believed that this value of Re marks the approximate onset of the strange saddle, and so, for Reynolds numbers lower than 1720 the probabilities of relaminarization depend on the history of the turbulent trajectory: the process is not memoryless, unlike the relaminarization process at $Re > 1720$.

Two different superexponential functional forms (obtained from data fitting) have been suggested for the escape rate.

- $\tau^{-1} = \exp[-\exp(c_1 Re + c_2)]$, with $c_1 = 0.0057$ and $c_2 = -8.7$
- $\tau^{-1} = \exp[-(Re/c)^n]$, with $c = 1549$ $n = 9.95$ (proposed by Tel & Lai in 2008 [27])

The impact of the mechanism to initiate the turbulent state on the relaminarization probabilities has been object of much debate in the literature (de Lozar & Hof 2008, Avila *et al.* 2009, etc). In order to establish if the type of perturbation used had an influence on the lifetime of the resulting turbulent flow, measurements were carried out at various amplitudes and different perturbation types.

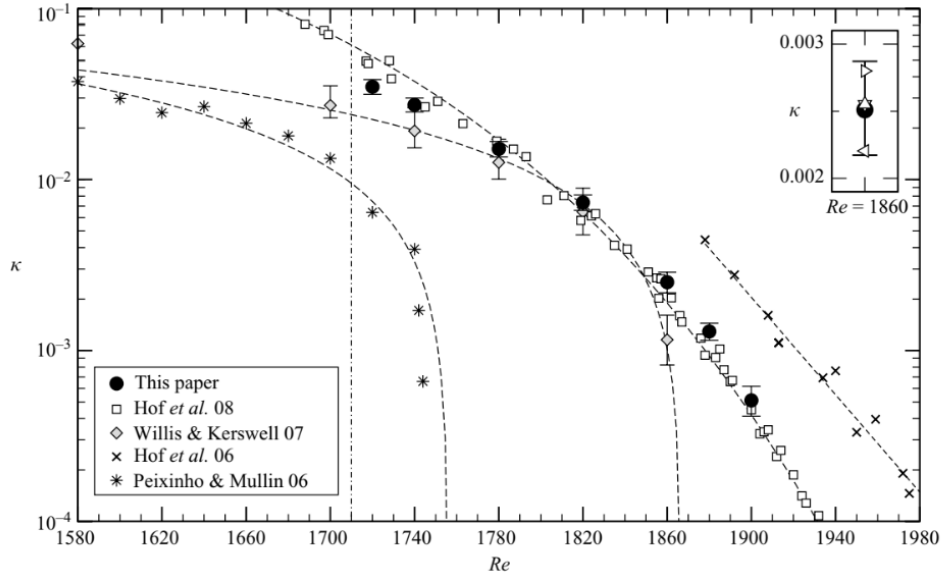


Figure 20: Escape rate $k = \tau^{-1}$ scaling with Re . The vertical line marks the approximate onset of the strange saddle. The inset shows the escape rate at $Re = 1860$: default reduction from $Re = 2000$ (black circle and 95% confidence interval), reductions from $Re = 2200, 1925, 1900$ (\triangle , ∇ , \triangleleft) and high numerical resolution (\triangleright). The dashed lines are a reproduction of the linear fit given by Willis & Kerswell and Peixinho & Mullin who considered τ as linear. From ref. [23]

Avila *et al.* (2010) [23] found out that all the additional cases render characteristic lifetimes within the 95% confidence interval about the default prediction (see inset of Fig.20), highlighting the independence of the lifetime statistics from initial conditions. These results confirm the experimental findings of de Lozar & Hof 2008 [22] who have demonstrated that outside the formation period t_0 , no differences, neither in the observed turbulent structures nor in their statistics are observed.

All these findings lead to a fundamental result (previously anticipated): in the turbulent regime no critical point exists and turbulence remains transient at all Reynolds numbers. The rapid exponential increase of lifetimes explains why the transient nature of turbulence has not been observed previously. Hof *et al.* estimate that to detect the decay of turbulence in a garden hose at a flow rate as low as 1 l/min ($Re = 2400$) would require a physical length of the tube of 40.000 km, about the Earth's circumference, and an observation time of almost 5 years. This implies that the turbulent and laminar states remain dynamically connected, suggesting avenues for turbulence control (Chapter 5).

5 How to eliminate turbulence

The observation that localized turbulent domains are intrinsically unstable offers prospects to control and relaminarize flows. Such potential methods are of great practical interest because the drag in turbulent flows is significantly larger and this causes higher energy consumption and limits transport rates.

Turbulence is the major cause of friction losses in transport processes and it is responsible for a drastic drag increase in flows over bounding surfaces.

5.1 Friction losses

As described in Chapter 1 (Section 1.3), losses due to friction in pipe flows are quantified by a dimensionless parameter called *Darcy friction factor* (equation (7)) which changes with the Reynolds number following Hagen-Poiseuille law (if the flow is laminar) and Blasius one (if the flow is turbulent and the pipe is smooth).

Thanks to their experiments, observing turbulent dynamics, Samanta, de Lozar and Hof (2011) [28] provided a well-defined link between the Hagen-Poiseuille and the Blasius law (respectively blue dashed line and red dashed line in Fig.21b)

They demonstrate that in the transitional regime the friction factor strongly depends on initial conditions as well as experimental imperfections, using two different obstacles: a small and a big obstacle (see Fig.21b, black stars and red squares). Furthermore, they investigate the dependence of f on initial conditions

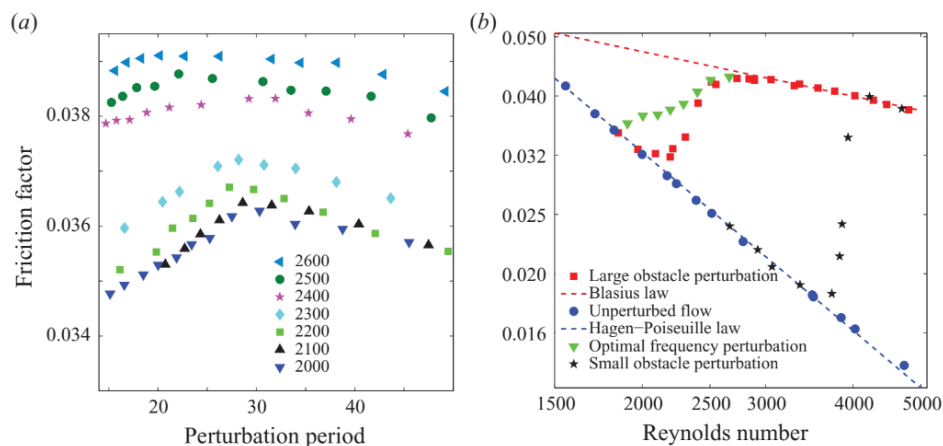


Figure 21: a) Friction factor as a function of the perturbation period. For $Re \leq 2300$, it is evident the presence of a maximum, i.e. the biggest density fraction of puffs. For $Re \geq 2400$ this maximum is no more distinguishable and this indicates that a fully turbulent flow state is approached. b) Friction factor as a function of Reynolds number using different perturbation types as indicated in the legend. Here we can clearly see a link between the Hagen-Poiseuille law (blue dashed line) and the Blasius law (red dashed line). From ref. [28].

and the puff interaction in spatially intermittent flows by applying periodic perturbations to the flow at a fixed position of the pipe used for the experiment. For small injection frequencies each perturbation results in a single puff, the rate of puff generation is in synchrony with the rate of injected perturbation and so the puff spacing is identical to the spacing preselected by the perturbation. However, for higher frequencies, new generated puffs interact and annihilate each other as supported by a previous study. This result is supported by Hof *et al.* (2010) [29], who found out that when puffs are located too close to each other the downstream puff decays.

As we pointed out in Chapter 2, turbulent structures propagates thanks to a self-sustained process, i.e. an amplification mechanism that constantly feeds energy from the mean shear into the turbulent eddies and vice versa. New vortices are generated through a nonlinear effect, such as inflectional instability. Indeed, across the interface the velocity profile adjusts from the upstream laminar parabolic shape to the average turbulent profile. This adjustment gives rise to inflection points in the velocity profile, fulfilling Rayleigh's inflection point criterion⁶, thus suggesting a hydrodynamic instability which drives the turbulent dynamics. So, when an upstream puff appears the inflection point behind the original puff is distorted and it is no longer capable of generating other vortices. Eventually the downstream puff decays if the distortion is strong enough.

The understanding of this process can be exploited to eliminate turbulence in spatially intermittent flows as we will explain in the following section.

In Fig.21a, it is displayed the friction factor as a function of the perturbation period. Starting from the right (big periods, small frequencies, large spacing) the friction factor is found to first increase with frequency and then reaches a maximum at the *optimum puff spacing*. Beyond this point the perturbed regions start to interact resulting in a lower density/packing fraction puffs.

While the maximum packing fraction is clearly differentiated for $Re < 2300$, the curves becomes flatter when increasing the Reynolds number until the point that the curves are almost flat ($Re = 2500$). The fading of the maximum indicates that a fully turbulent flow state is approached.

The maximum packing fraction data provide an upper bound for the friction factor for a given Reynolds number, shown by the green triangles in Fig.21b.

5.2 Turbulence control strategies

It has been experimentally demonstrated for pipe flow that appropriate distortions to the velocity profile lead to a complete collapse of turbulence and subse-

⁶**Rayleigh's inflection point criterion:** a necessary condition for instability is that the basic velocity profile should have an inflexion point

quently friction losses are reduced by as much as 95%.

Generally, the flatter the velocity profile the more the streak vortex interaction is suppressed, and in the limiting case of a uniformly flat profile the lift up mechanism breaks down entirely. Hence, the fully turbulent state can be destabilized by forcing the velocity profile, i.e. blunting it to a more plug-like form.

Recent strategies employ feedback mechanisms to actively counter selected velocity components or vortices. Such methods usually require knowledge of the full turbulent velocity field and can be applied exclusively in computer simulations. In experiments the required detailed manipulation of the time dependent velocity field is, however, currently impossible to achieve.

Counterintuitively, the return to laminar motion is accomplished by initially increasing turbulence intensities or by transiently amplifying wall shear. In this Section, we present some methods which can be used to relaminarize turbulence by applying appropriate perturbations (see Kühnen *et al.*, 2018 [30,31]).

To achieve a similar effect in experiments one way is to increase the turbulence level by vigorously stirring a fully turbulent pipe flow ($Re = 3500$), employing four rotors located inside the pipe. As the highly turbulent flow proceeds further downstream it surprisingly does not return to the normal turbulence level but instead it quickly reduces in intensity until the entire flow is laminar. (see Fig.22, red circle).

In a second experiment, turbulent flow ($Re = 3100$) is disturbed by injecting fluid through 25 small holes (0.5 mm diameter) in the pipe wall. When the perturbation is actuated downstream fluctuation levels drop and the centre line velocity returns to its laminar value. In this case, the kinetic energy required for relaminarization (including the actuation and the drag increase in the control section) is only 2.6% of the energy saved because of the drag decrease in the remainder of the pipe and the net power saving amounts to 45% (see Fig.22, purple triangle).

In another experiment Kühnen *et al.* [30] attempted to disrupt turbulence ($Re = 5000$) by injecting fluid parallel to the wall in the streamwise direction. Unlike for the previous case, this disturbance does not result in a magnification of cross-stream fluctuations, but instead increases the wall shear stress and hence also the friction Reynolds number, Re_τ . Even though this local increase in shear stress, this control is more effective as a net power saving of 55 % and more can be achieved (see Fig.22, black squares).

In order to test a possible connection between the initial flat velocity profile and the subsequent turbulence collapse, computer simulations has been carried out. In these simulations, volume force was added to the full Navier-Stokes equations. Unlike in the experiments where the disturbance is applied locally

and persists in time, here the forcing is applied globally. Upon turning on the forcing with sufficient amplitude, a net energy saving is already obtained in the presence of the forcing (in experiments the saving is achieved downstream of the perturbation location). As we can see in Fig.22 (green triangles) in this case the energy saving is up to 95%.

In the last experiment carried out by Kühnen *et al.* (2018) [30] profiles has been flattened by a local change in the boundary conditions, since body forces like that used in the simulations are not available in practice (at least not for ordinary, non-conducting fluids). For this purpose one pipe segment is replaced by a pipe of slightly (4%) larger diameter which is pushed over the ends of the original pipe and can be impulsively moved with respect to the rest of the pipe. The impulsive acceleration of the near wall fluid leads to a flattened velocity profile. This last method can be considered the most efficient, as it can be obtained a drag reduction up to 90%.

In summary it has been shown that fully turbulent flow can be destabilized by appropriate perturbations. As a consequence the entire flow becomes laminar, drastically reducing friction losses and key to relaminarization is a rearrangement of the mean turbulent profile that inhibits the vortex streak interaction.

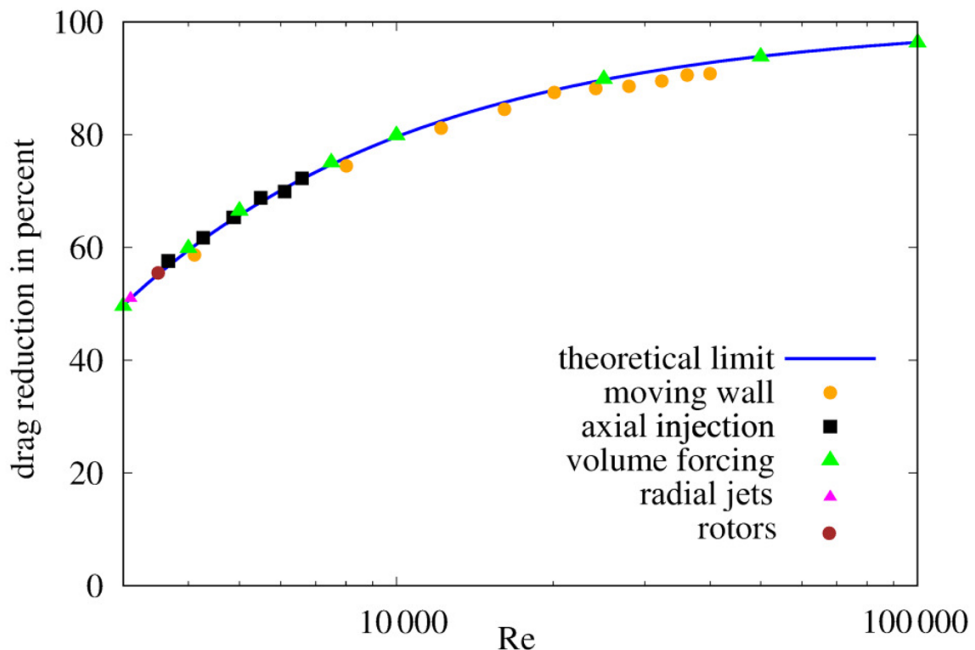


Figure 22: *Drag reduction as a function of Re . For the injection perturbation a maximum drag reduction of $\sim 70\%$ was reached whereas for the moving wall and volume forcing 90 and 95% were achieved respectively. From ref. [30]*

6 Conclusions

The past decades have seen much progress in our understanding of the transition to turbulence in shear flows without linear instabilities.

In this report, we have tried to summarize and explain all the recent findings, in a way as clear as possible.

Our main sources, covering a very long period (from 1970s to 2018), have allowed us to realize how much progress has been made and also how many questions are still needed to be answered.

We have analyzed the entire "life" of the fundamental turbulent structures and we have highlighted the strong dependence on Reynolds number, which characterizes every aspect of the flow structure and can be thought as the guideline for the entire process.

One way to summarize the different processes and transitions is the sequence of Reynolds numbers shown in Fig.23. It will be interesting to explore similar sequences and processes in other flows.

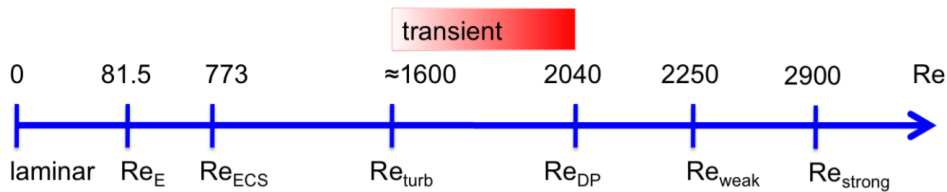


Figure 23: *The various Reynolds numbers of pipe flow along the Reynolds number axis (not to scale): energy stability $Re_E = 81.5$; appearance of the first critical states near $Re_{ECS} = 773$; first indications of turbulence in experiments near $\simeq 1600$; critical Reynolds number from balance between splitting and decay $Re_{DP} \simeq 2040$; weak spreading of slugs above $Re \simeq 2250$; and finally transition to strong spreading near $Re = 2900$. From ref. [19].*

In Chapters 2,3 and 4, all the recent knowledge about transition to turbulence in pipe flow has been collected: how turbulent patches rise, what their structure is and how they spread, splitting or spreading, and eventually how they generate turbulence.

Turbulence has been found in pipe despite the stability of the base laminar flow and first takes the form of localized patches, which are transient (with a lifetime that goes to infinity asymptotically for $Re \rightarrow \infty$). Furthermore, it has been pointed out the strong non-linear instability that characterize the process and can be understood thanks to the dynamical system theory. Although much progress has been made in our understanding of how turbulence in wall-bounded flows is formed from unstable invariant solutions (*travelling waves*) at moderate Re , little to no progress has been made in connecting this transitional regime to studies of

high- Re turbulence. Explaining the origin of the fully turbulent state is a decisive step towards connecting these regimes and paves the way for a bottom-up approach to turbulence.

A critical aspect of the generation of puffs and slugs is the self-sustained process, whose understanding has been fundamental in order to clarify the birth mechanism and to develop methods useful to eliminate turbulence. As shown, relaminarization can be achieved in a variety of ways, offering a straightforward target for practical applications where potentially pumping and propulsion costs can be reduced by 95% or more. The future challenge is to develop and optimize methods that lead to the desired profile modifications in high Reynolds number turbulent flows.

A Appendix

EXPERIMENT DESCRIPTION

Here it is described the experimental apparatus used by Hof *et al.* in 2004 and in 2006 (with some upgrades). This set-up forms the basis for the more recent experiments, in which further technical improvements have been added.

A schematic of the experimental set-up is shown in Fig.24. Fully developed laminar pipe flow (i.e., for which the velocity profile was parabolic) was generally destabilized 350 pipe diameters from the inlet by means of injecting an impulsive jet for 1.5 s ($\simeq 1.9D/U$) through a hole of 1-mm diameter in the pipe wall. The jet was injected orthogonally to the main flow with a volume flux of approximately 50% of the flux in the pipe. The so-created turbulent flow region was inspected 150 pipe diameters downstream of the injection point with a high-speed stereoscopic particle image velocimetry (PIV) system. Here a cross-sectional plane of the pipe is illuminated with a laser light sheet using a pulsed Nd:YLF (Neodymium-doped: Yttrium Lithium Fluoride) laser and this plane is viewed with two 500 Hz cameras positioned in forward scatter on opposite sides of the light sheet at 45° to the observation plane. As found in previous observations a distance of $150D$ is more than sufficient to allow all transients inflicted by the perturbation mechanism to subside. For visualization purposes, the water was seeded with $10\ \mu\text{m}$ tracer particles that were neutrally buoyant and illuminated by the frequency-doubled pulsed laser. The full three-component velocity field at about 2600 points in the observation plane was reconstructed from the displacement of the tracer particles between subsequent images recorded by the cameras. The passage of turbulent structures was recorded in a series of 1000 contiguous measurements at sampling frequencies between 60 and 500 Hz. A high degree of precision (figs. S4 to S8) was achieved with the use of a test section that minimizes optical distortion and an optimized calibration procedure to align the stereoscopic camera set-up.

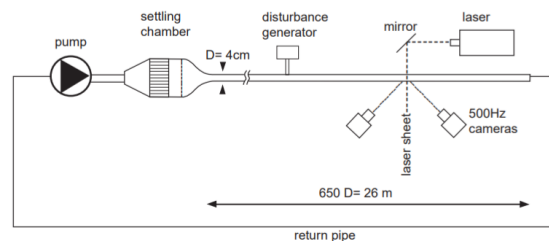


Figure 24: *Experimental apparatus. Water is pumped by way of a settling chamber into a 26-m-long straight pipe that has a diameter of $D = 4\text{ cm}$. The settling chamber as well as the inlet shape were designed to minimize disturbances from the inlet. The entire pipe is thermally insulated to avoid heat convection, which would distort the flow profile. From ref. [5].*

References

- [1] O. Reynolds, Proc. R. Soc. London 35, 84 (1883).
- [2] J.D. Anderson, Jr. Fundamentals of Aerodynamics (2007).
- [3] R. Arina, Fondamenti di Aerodinamica (2015).
- [4] D.J. Tritton, Physical Fluid Dynamics, (1988).
- [5] B. Hof, C. van Doorne, J. Westerweel, F. Nieuwstadt, H. Faisst, B. Eckhardt, H. Wedin, R. Kerswell, and F. Waleffe, Science 305, 1594 (2004).
- [6] B. Hof, C. van Doorne, J. Westerweel, and F. Nieuwstadt, Phys. Rev. Lett. 95, 214502 (2005).
- [7] J. Hamilton, J. Kim, and F. Waleffe, J. Fluid. Mech. 287,317 (1995).
- [8] F. Waleffe, Phys. Fluids 9, 883 (1997).
- [9] B. Hof, A. Juel, and T. Mullin, Phys. Rev. Lett. 91, 244502 (2003).
- [10] A.G. Darbyshire and T. Mullin J. Fluid Mech 289, 83-114 (1995).
- [11] B. Eckhardt, T. Schneider, B. Hof, and J. Westerweel, Annu. Rev. Fluid Mech. 39, 447 (2007).
- [12] K. Avila, D. Moxey, A. deLozar, M. Avila, D. Barkley, and B. Hof, Science, 333, 192 (2011).
- [13] D. Barkley, B. Song, V. Mukund, G. Lemoult, M. Avila and B. Hof, Nature (London) 526, 550 (2015).
- [14] B. Song, D. Barkley, B. Hof, and M. Avila J. Fluid Mech. (2017) vol. 813, pp. 1045-1059
- [15] A.P. Willis, J. Peixinho, R.R. Kerswell, and T. Mullin, Philosophical Transactions of the Royal Society A: Mathematical, Physical and Engineering Sciences (2008).
- [16] I.J. Wygnanski and F.H. Champagne, J. Fluid Mech. 59, 281–335 (1973).
- [17] S. B. Pope, Turbulent flows. Cambridge university press (2000).
- [18] John W. Milnor, Attractor. Scholarpedia, 1(11):1815 (2006).
- [19] B. Eckhardt, Phys A: Stat Mech App., 504, pp. 121-129 (2018).
- [20] E. Ott E. Chaos in Dynamical Systems. Cambridge, UK: Cambridge Univ. Press (1993).
- [21] B. Hof, J. Westerweel, T. Schneider, and B. Eckhardt, Nature (London) 443, 59 (2006).
- [22] B. Hof, A. de Lozar, D. J. Kuik, and J. Westerweel, Phys. Rev. Lett. 101, 214501 (2008).
- [23] M. Avila, A. Willis, and B. Hof, J. Fluid Mech. 646 121 (2010)
- [24] H. Faisst and B. Eckhardt, Journal of Fluid Mechanics, 504, 343-352 (2004).

- [25] T. Mullin, and J. Peixinho, *J Low Temp Phys* 145: 75 (2006).
- [26] A. Willis, and R. Kerswell, *Phys. Rev. Lett.* 98, 014501 (2007).
- [27] T. Tel and Y.-C. Lai, *Phys. Rep.* 460, 245 (2008).
- [28] D. Samanta, A. de Lozar, and B. Hof, *J. Fluid Mech.* 681, 193-204 (2011)
- [29] B. Hof, A. de Lozar, M. Avila, X. Tu, T. M. Schneider, *Science*, 327, (2010).
- [30] J. Kühnen, B. Song, D. Scarselli, N. Burak Budanur, M. Riedl, A. Willis, M. Avila, B. Hof, *Nature Physics*, 14.10.1038 (2018).
- [31] J. L. Lumley, P. Blossey, Control of turbulence. *Ann. Rev. Fluid Mech.* 30, 311 (1998).
- [32] A. de Lozar, F. Mellibovsky, M. Avila and B. Hof, *Phys. Rev. Lett.* 108, 214502 (2012).
- [33] M. Avila, F. Mellibovsky, N. Roland and B. Hof, *Phys. Rev. Lett.* 110, 224502 (2013).